




Multiferroic and optical characteristics of $\text{Mg}_2(\text{Fe}_{0.85}\text{Ni}_{0.15})\text{NbO}_6$ for possible energy storage application

S. Mohanty¹, Santanu Sen³, S. Behera^{2,*}, and B. N. Parida^{3,*} 

¹Department of Physics, Trident Academy of Technology, Bhubaneswar 751024, India

²Department of Physics, Centurion University of Technology & Management, Bhubaneswar, Odisha 752050, India

³Department of Physics, Central Institute of Technology Kokrajhar, (Deemed to Be University, MoE, Govt. of India), BTR, Assam 783370, India

Received: 2 May 2022

Accepted: 13 September 2022

Published online:

1 October 2022

© The Author(s), under exclusive licence to Springer Science+Business Media, LLC, part of Springer Nature 2022

ABSTRACT

Alkaline earth-based double perovskite composites are novel perovskite compounds that have been the recent topic of interest for many material physicists. Since not much work has been reported in this particular field of study; hence, we took up the task of analyzing the multifunctional and multiferroic properties of $\text{Mg}_2(\text{Fe}_{0.85}\text{Ni}_{0.15})\text{NbO}_6$. The frequency-dependent dielectric, impedance, and tangent loss characterizations were performed to infer the capacitive and semiconducting properties of the sample. The magnetic study revealed the weak ferromagnetic characteristics of the composite, particularly induced by structural distortions. The nonzero P–E hysteresis loop at room temperature indicates the ferroelectric polarizations present in the compound. The optical band gap was estimated by extrapolating the Tauc plot of ultraviolet–visible spectroscopy covering the UV to the visible range of the electromagnetic spectra. The conductivity analysis was performed following the frequency-dependent ac conductivity which showed very good high-frequency ac conductivity of the ceramic.

1 Introduction

Double perovskite compounds with divalent alkaline earth elements at the A site and heterovalent elements at the B site are emerging composite compounds in the material science community due to their metallic, half metallic, high ferroelectric, and magnetic transition temperatures. Such compounds

are commonly expressed by the chemical notation $\text{A}_2\text{B}'\text{B}''\text{O}_6$ or $\text{A}_2(\text{B}'_{1-x}\text{B}_x'')\text{O}_6$. Since very few works have been reported in this field, hence extensive research and development are needed in this field of study. Out of the very few results which have been reported in the recent times, few show very promising outcomes. (Re)-based DP oxides such as A_2FeReO_6 , where $A = \text{Ba}/\text{Sr}/\text{Ca}$ were analyzed

Address correspondence to E-mail: saubhagyalaxmi.behera@cutm.ac.in; bichitra72@gmail.com

recently due to their dielectric behaviors, and promising carrier spin polarization [1]. $\text{La}_2\text{FeReO}_{6+\delta}$ (LFRO) solid powders synthesized by solid-state reaction route resulted in promising high Curie temperature ferromagnetism and relaxor orientational polarizabilities [2]. In the recent times, magnetic investigations on $\text{Sr}_2\text{CaIrO}_6$ inferred an antiferromagnetic ordering below $T_N = 58$ K and 74 K for $\text{Sr}_2\text{MgIrO}_6$ [3]. The results of the dielectric investigations of Ba_2MeWO_6 (Me = Mg, Ni, Zn) Double Perovskites were reported by D Khalyavin et al. which showed that charge distributions among the B cationic site atoms have a significant influence on the temperature-dependent dielectric constant of the compound [4]. Sr_2MMoO_6 Double Perovskite where M as Ni or Mg or Fe were also investigated and it exhibited the properties of promising anode materials for solid oxide fuel cells [5]. Further investigation on halide-based double perovskites such as $\text{A}_2\text{AgRhCl}_6$ (A = K, Rb, and Cs) showed its potential photoelectric applications due to its absorption ability in the region covering the range 1.0–4.5 eV [6]. The optical analysis on $\text{Cs}_2\text{Na}_x\text{Ag}_{1-x}\text{BiCl}_6$ for $x = 0, 0.25, 0.5, 0.75, 1$ double perovskites resulted in increase in optical band gap from 3.39 eV for $x = 0$ to 3.82 eV for $x = 1$ with 30-fold increment in weak photoluminescence, useful for photo-catalytic applications [7]. $\text{Pr}_{2-x}\text{Sr}_x\text{MgIrO}_6$ double perovskites, for $x = 0.5$, showed that AFM transition takes place to a much lower temperature $T_N \sim 6$ K due to weakening of the AFM super-exchange interactions [8].

Sr_2MirO_6 , with M, as Ca/Mg resulted in spin–orbit coupling, mediated by long-range magnetic exchange interactions [9]. Magnetic susceptibility measurements were performed on doped DPO $\text{Sr}_2\text{Ni}_{1-x}\text{Mg}_x\text{MoO}_6$ with $x = 0.25, 0.5$. For $x = 0.25$, the composite was antiferromagnetically ordered below 56 K whereas, for $x = 0.5$, the compound showed paramagnetism [10]. Hence, we chose our aforementioned sample to undergo dielectric, optical, and electrical characterizations to look for applicable outcomes. The importance as well as the motivation behind the choice of the studied composition is based on the fruitful applicable results of the earlier similar works done on Mg, rare-earth (RE), and Fe/Ni-based double perovskites, which are cited above as the literature surveys. The present study reflects the multiferroic and optical characteristics of

$\text{Mg}_2(\text{Fe}_{0.85}\text{Ni}_{0.15})\text{NbO}_6$ for devices, such as multilayer capacitor, memory devices perovskite solar cell etc.

2 The composite synthesis route

Conventional solid-state reaction mechanisms were followed while carrying out the synthesis process of the nanocomposite. Proper stoichiometric proportions of MgCO_3 , Fe_2O_3 , Ni_2O_3 , and Nb_2O_5 compounds were mixed and extensively grind together in dry as well as the wet environment, followed by the calcination of the compound under repeated heating process till the formation of the $\text{Mg}_2(\text{Fe}_{1-x}\text{Ni}_x)\text{NbO}_6$ composite. The composite was then taken in a Pt. crucible and calcined at around 1235 °C for 11 h and then brought back to the ambient temperature under natural slow cooling. The calcinated composite powder was then characterized by the X-ray diffraction method to check the formation of the crystallites. After that the compound was palletized into cylindrical discs having a thickness of the order of 2–3 mm and of 10 mm in diameter, using Poly Vinyl Alcohol as an adhesive binder to reduce the ceramic's fragileness, which was later evaporated out during high-temperature sintering at 1280 °C for 6 h and then again cooling it down to the ambient condition. The sintered pellets were then polished to make both their faces smooth, following that electroding by high purity silver paste, and then connected to the LCR meter and other instruments for the characterizations.

2.1 The analytical approaches

The optical band gap was calculated in the spectral range of 200–800 nm and was done using the Shimadzu-2600 UV–Visible spectrophotometer. An integrating sphere coded ISV-922 of 60 mm size was used to minimize the diffusion/scattering of radiation. The frequency–reliant dielectric and impedance analysis was executed using an LCR meter model: PSM 1735, N4L-LCR (UK origin) in the frequency sweep of 1 kilo Hz to 1 Mega Hz and temperature interval of 25 °C–500 °C. Keithly 2400 standard series SMU I-V meter was employed to investigate the presence of pyroelectric properties, semiconducting nature, and activation energies. Lake Shore 7400 series VSM was incorporated to analyze the room temperature M–H loop of the composite with

1×10^{-7} emu noise floor at 10 s/pt, 7.5×10^{-7} emu noise floor at 0.1 s/pt, with applied fields up to 3 T.

3 Analytical findings

3.1 Structural and elemental findings

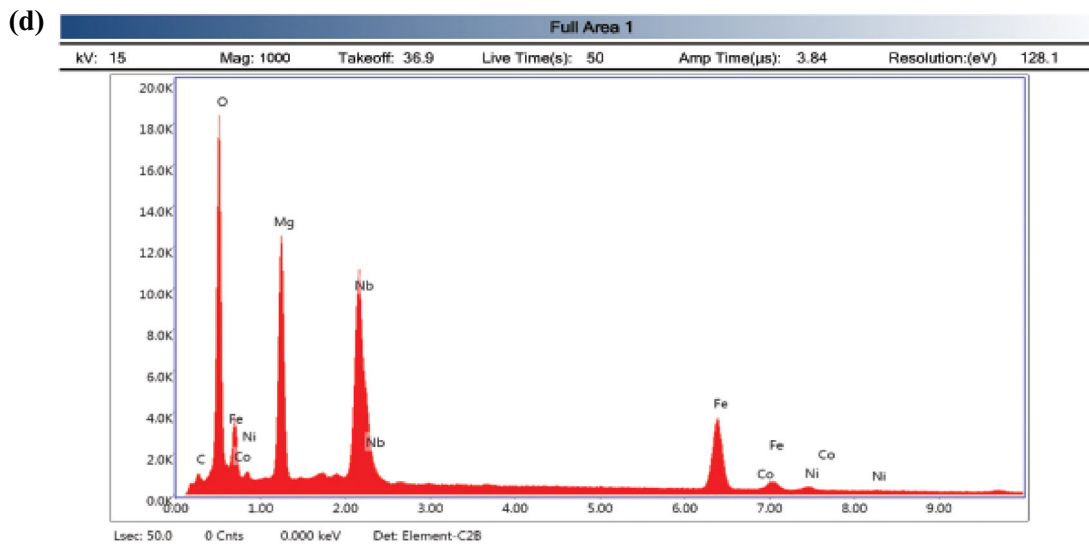
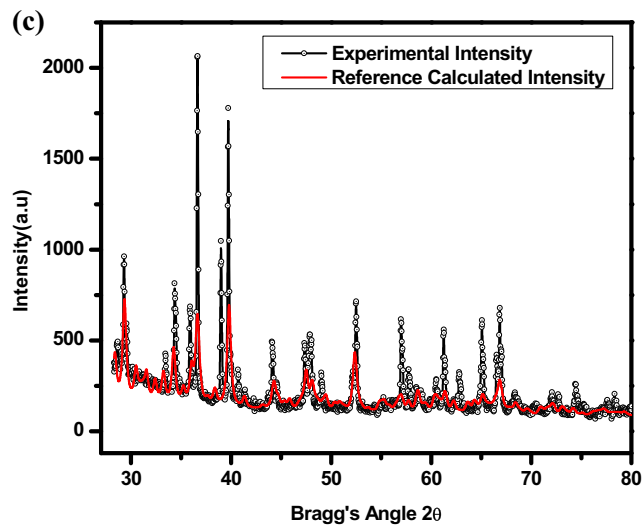
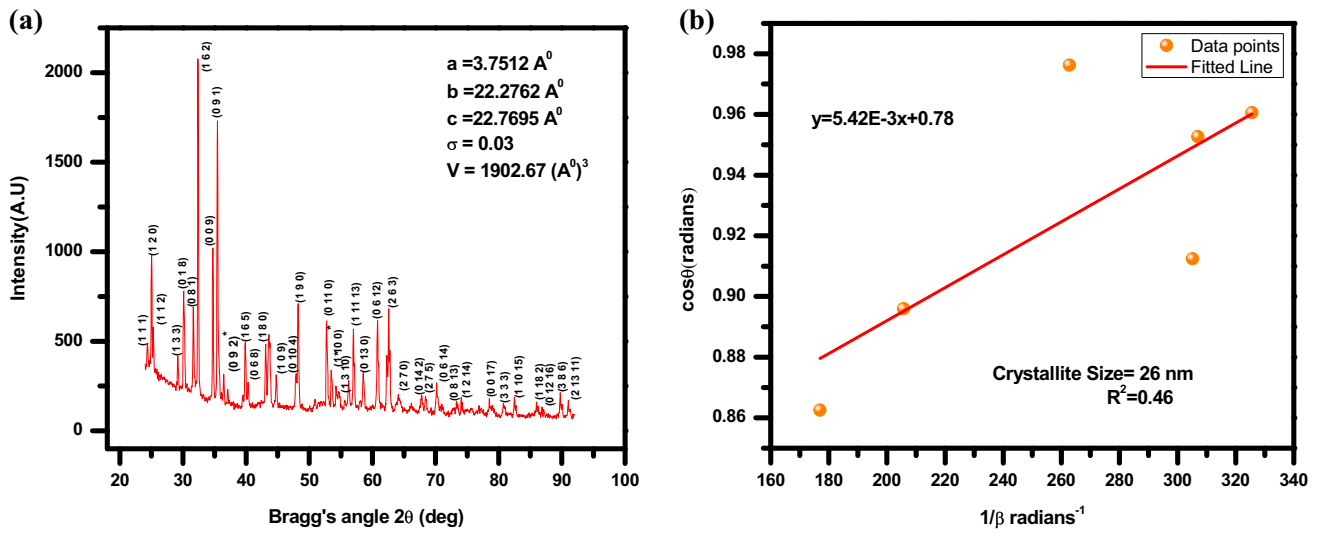
The commercially available POWD refinement software was employed to investigate the species of the lattice structure, lattice parameters, and d values corresponding to each peak of the investigated XRD profile as shown in Fig. 1a. The most preferred direction of crystal growth can be estimated from the miller indices of directions belonging to the maxima peak is (1 6 2) and the values of the d -spacing along with the miller indices for all the indexed peaks are tabulated in Table 1. The crystal structure was found to be belonging to the orthorhombic class of bravais lattice having the crystal structure parameters as $a = 3.7512 \text{ \AA}^0$, $b = 22.2762 \text{ \AA}^0$, $c = 22.7695 \text{ \AA}^0$, with volume $V = 1902.67 (\text{ \AA}^0)^3$ and $\sigma = 0.03$. The crystalline size was determined from the $\cos \theta$ versus $1/\beta$ plot as shown in Fig. 1b. The crystallite size, δ (say) was determined by evaluating the slope of the $\cos \theta$ versus $1/\beta$ plot following the Debye–Scherrer relation $\cos \theta = \frac{\kappa \lambda}{\delta} \beta^{-1}$ [11], where $\frac{\kappa \lambda}{\delta}$ = slope of the fitted straight line and $\kappa = 0.89$. The crystallite size (δ) was estimated to be 26 nm. Figure 1c displays the best fit of the calculated reference pattern to the experimental pattern, performed via Rietveld refinement. The refinement operation identified the lattice distortion arrangement as an orthorhombic arrangement, with Pnmm: 2cab space group. Figure 1d demonstrates the EDAX spectra, particularly performed to delineate information regarding the elemental presence of the formed compound. As it is clearly visible from the plot that all the possible precursor elements are present in the studied compound, with their relative percentage strengths being represented by the peak intensities.

3.2 Dielectric permittivity and $\tan \delta$ findings

The field(frequency)-dependent dielectric and dielectric loss analysis and its findings in the frequency domain (1 kHz–1 MHz) are depicted in Fig. 2a and b. The real part of the dielectric constant (ϵ') and then dielectric loss (ϵ'') were evaluated and

the dielectric loss tangent ($\tan \delta$) using the formulae Smit and Wijnet. al. [12] $\epsilon' = \epsilon''(\tan \delta)^{-1}$. It is visible from Fig. 2a that the dielectric permittivity exhibits some dispersion behavior in the low-frequency range. This may be assigned to the orientational polarizability due to the out phase response to the applied field and due to the space charge polarizability of the ceramic, arising due to the nonmobility of the charge carriers at the grain walls [13]. Dipolar and space charge relaxation mechanisms might also be held responsible for the dispersive nature of the value of the dielectric parameter. The composite structure is made up of a continuous or discontinuous array of electrically conducting grains, which are separated from each other by nonconducting insulating grain walls, acting like a Schottky kind of barrier. Under the influence of electrical perturbations, the mobility of charge carriers in grains is obstructed at grain boundaries. This results in localization and accumulation of space charge at the grain discontinuity, which causes interfacial polarization. The dielectric values at higher frequencies show negligible changes and hence saturate to minimum fixed values. The explanation of such behavior might be explained based on Koop's phenomenological idea [14]. According to the aforesaid approach, the saturation of polarization with enhancing frequency might be attributed to the fact that when a certain frequency of the electric field is exceeded, the electronic exchange interactions between Fe^{2+} and Fe^{3+} cannot respond to and follow the applied perturbing field, hence dielectric parameter ϵ_r falls to minimum values. The enhancement in the dielectric values with temperature is brought in by the enhanced short-range hopping mechanisms between the ferrite valency fluctuations due to the large concentration of oxygen vacancies generated due to the temperature rise.

The dielectric loss and hence the $\tan \delta$ arise due to the polarization lag between the applied perturbing field and space charge/dipolar systems. Usually, at low frequency, ϵ' is high but ϵ'' is low. This helps in dispersing the values of $\tan \delta$, irrespective of the temperature. Also, the presence of various impurities and defects in the crystal causes the polarization lag. The relaxation mechanism, at a fixed frequency known as the relaxation frequency, corresponds to this relaxation behavior mediated by the polarization lag. This relaxation behavior has been explained by



◀ **Fig. 1** **a** The X-ray diffraction profile. **b** $\cos \theta$ vs. $1/\beta$ plot. **c** The reference fitted plot from Rietveld refinement. **d** The EDAX spectra for elemental analysis

Rezlescu [15]. The model depicts that the relaxation behavior is obtained when the frequency of charge hopping between the Fe^{2+} and Fe^{3+} exactly matches the frequency of the externally applied field. The condition for maxima in the dielectric losses of dielectric material is given by the relation. The relaxation time is related to the jumping/hopping

probability per unit time, given by p and related by the equation $\tau \propto p^{-1}$.

3.3 Optical spectroscopy from UV–Visible spectra

The absorbance plot and the corresponding tauc plot are useful tools to delineate the optical energy gap of the compound under study. The optical band gap was calculated from the linear extrapolation of the energy-dependent Tauc plot of the absorption spectra using an appropriate function, corresponding to direct-allowed transition. Figure 3a shows the

Table 1 The POWD refinement parameters

Line	Observed inter planer Spacing (d_{obs})	Calculated inter planer Spacing (d_{cal})	h k l indices
1	3.6512	3.6512	(1 1 1)
2	3.550	3.550	(1 2 0)
3	3.5181	3.5181	(1 1 2)
4	3.0583	3.0634	(1 3 3)
5	2.8263	2.8232	(0 1 8)
6	2.7644	2.7639	(0 8 1)
7	2.5814	2.5706	(1 6 2)
8	2.5301	2.5299	(0 0 9)
9	2.4634	2.4606	(0 9 1)
10	2.4226	2.4186	(0 9 2*)
11	2.2805	2.2832	(1 6 5)
12	2.2607	2.2588	(0 6 8)
13	2.2364	2.2358	(1 8 0)
14	2.0981	2.0975	(1 0 9)
15	2.0744	2.0744	(0 10 4)
16	2.0675	2.0659	(1 9 0)
17	2.0236	2.0251	(0 11 0)
18	1.9127	1.9153	(1 10 0*)
19	1.8854	1.8828	(1 3 10*)
20	1.7349	1.7348	(1 11 3)
21	1.7128	1.7136	(0 13 0)
22	1.6901	1.6896	(0 6 12)
23	1.6345	1.6348	(2 6 3)
24	1.6148	1.6158	(2 7 0)
25	1.5758	1.5758	(0 14 2)
26	1.5221	1.5228	(2 7 5)
27	1.4901	1.4897	(0 6 14)
28	1.4830	1.4826	(0 8 13)
29	1.4792	1.4790	(1 2 14)
30	1.3401	1.3394	(0 0 17)
31	1.2172	1.2171	(3 3 3)
32	1.1894	1.1897	(1 10 15)
33	1.1686	1.1690	(1 18 2)
34	1.1296	1.1294	(0 12 16)
35	1.0919	1.0924	(3 8 6)
36	1.0799	1.0794	(2 13 11)

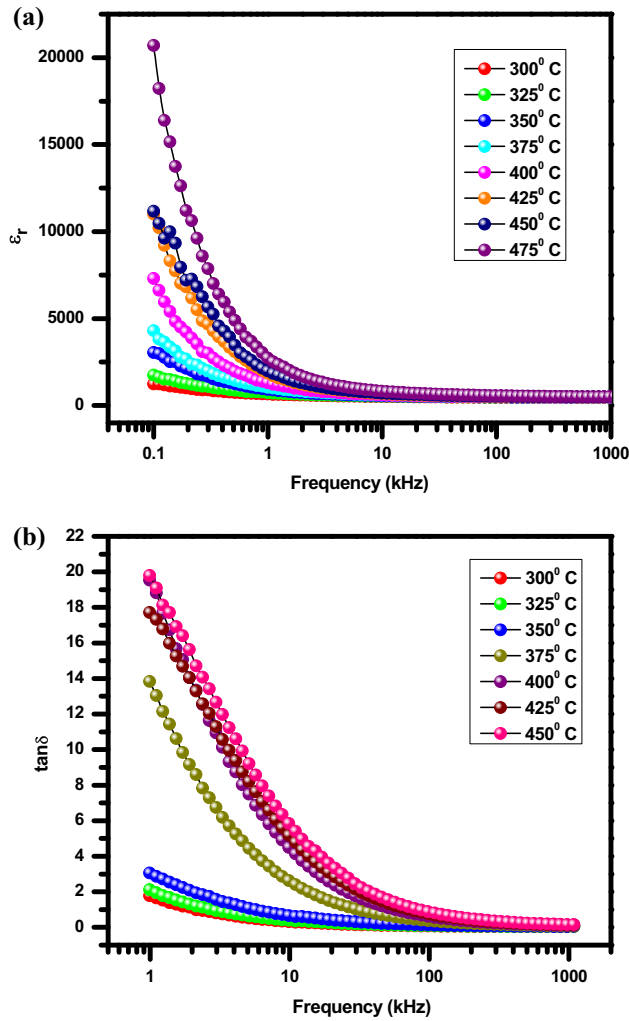


Fig. 2 a Dielectric constant vs. frequency. b Tangent loss vs. frequency

absorption spectra and the intercept value on the wavelength axis which is roughly equal to 712.25 nm. The absorbance curve also shows that the sample’s absorbance tends to reach the maxima between 350 and 400 nm, which usually corresponds to the visible band of spectra. The curve is also exhibiting peaks at the wavelength values of around 480 nm and 550 nm which belong to the UV part of the E–M radiation. This implies the sample’s potential applicability in visible and UV radiation sensing devices. The energy gap E_g was measured for all samples using the Tauc plot method, according to the proportionality relation among $(\alpha hv)^2$ vs. hv [16]. The possibility of direct transition has been considered here for which the value $n = 1/2$. The value of the optical band gap was

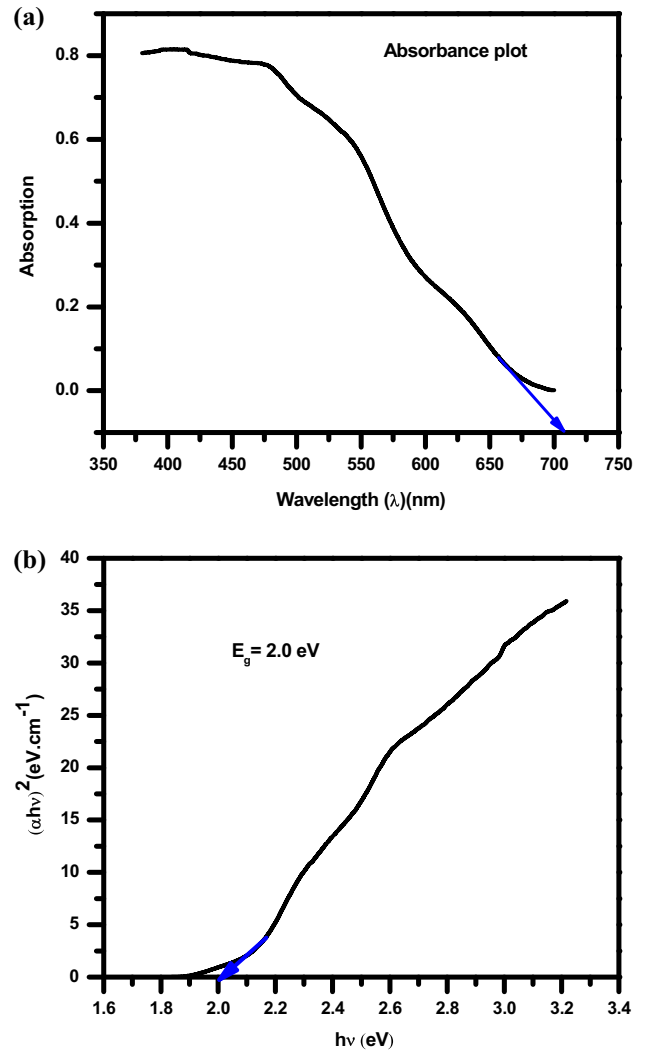


Fig. 3 a The UV absorbance. b Tauc plot for band gap estimation

found to be approximately 2.05 eV, as evident from Fig. 3b.

4 The real impedance and the imaginary (capacitive) impedance spectroscopy (CIS)

The cumulative bulk grain and grain boundary contributions towards resistive as well as capacitive effects, following the temperature-dependent conductivity and the possible NTCR behavior of the composite can be revealed by employing the CIS method. The frequency-dependent behavior of the real impedance Z' concerning the applied sinusoidal field, at some selected temperatures, is depicted in Fig. 4a. The Z' values have maximum saturated

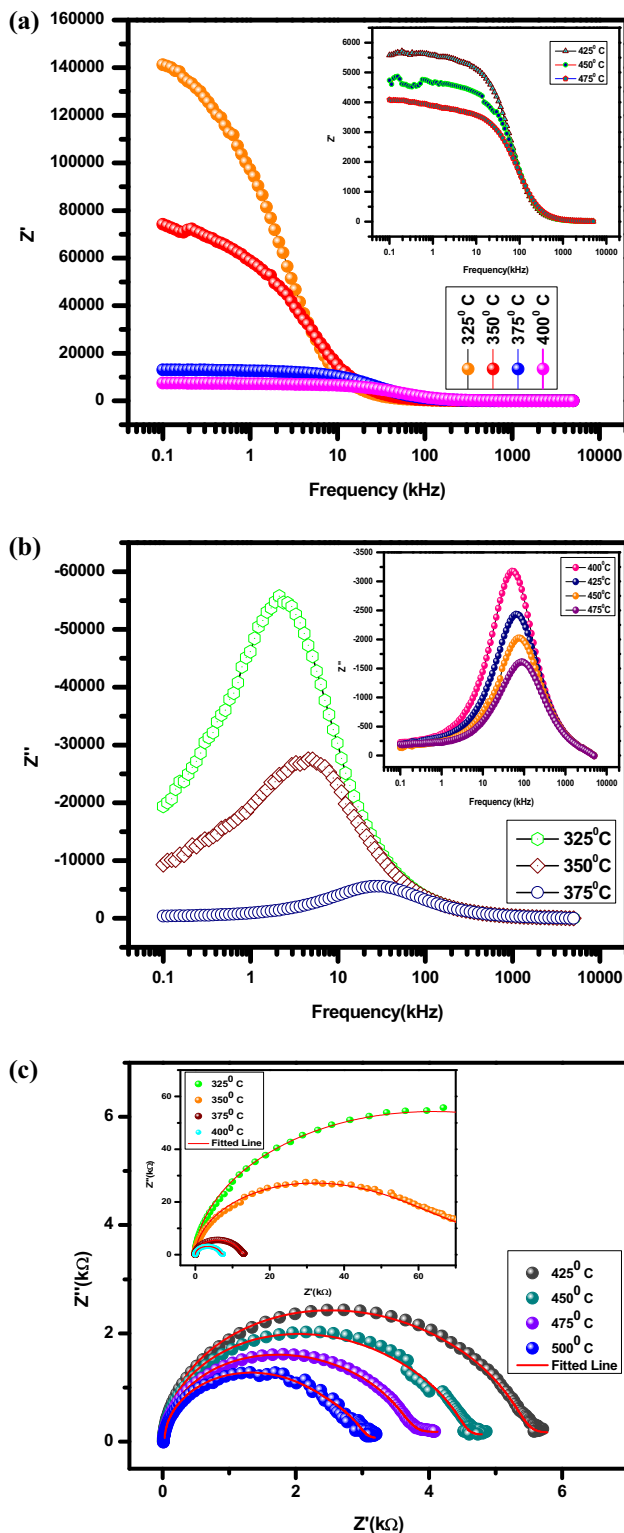


Fig. 4 a Variation of real impedance (Z') with frequency. b Imaginary impedance (Z'') vs. frequency. c The Cole–Cole plot

values at lower frequencies, which then saturate to minimum values at higher frequencies. This suggests the dominance of short-range polarizations, hopping mechanisms, and grain boundary barriers at low frequency. The fall in Z' values at higher frequencies indicate the dominance of ac conductivity at higher temperatures. The existence of NTCR nature in the composite is evident from the decreasing maximum values Z' with the temperature rise. The relaxation mechanisms in Z'' plot with increasing frequency and at different temperatures are enumerated in Fig. 4b. The amplitude of the relaxation peaks is seen to decrease with the rise in temperature, which validates the existence of NTCR again. Because the relaxation peaks continuously shift towards the right with the temperature rise, hence, it reflects the temperature-dependent relaxation mechanisms of the relaxors, where the relaxation time is found to be decreasing with the temperature rise following the relation $\tau_m = \omega_m^{-1}$. Figure 4c shows the angular frequency dependence of $Z'(\omega)$ and $Z''(\omega)$ of the DPO as a function of temperature. This plot is generally known as the Cole–Cole or argand plot, a plot of semicircular arcs whose intercept values give the grain or grain boundary contributions towards real impedances. The values of real impedance (R) and the capacitance (C) values can be extrapolated using an equivalent parallel RC network. This RC network gives rise to one semicircle or two arcs or three arcs on the argand plane plot, representing the grain effect, grain boundary, and electrode effects. However, a departure from the ideal Debye type behavior, especially when the semicircles are depressed ones, the RC network needs to be parallel connected to a constant phase element to account for the depression. The equivalent electrical equations for grain are [17]

$$Z' = \frac{R + R(\omega R_g C_g)^2 + R_g}{1 + (\omega R_g C_g)^2}, \quad Z'' = \frac{\omega R_g^2 C_g}{1 + (\omega R_g C_g)^2}.$$

In the temperature sweep from 325 to 400 °C, we are getting single semicircles representing the grain effects on capacitance and resistance values. Its intercept values are in decreasing trend as the temperature rise denoting the existence semiconducting nature in the DPO ceramic. From 425 °C onwards, a second semicircle tries to appear which denotes the feeble contributions arising from the grain wall effects at higher temperatures.

4.1 The frequency-dependent complex modulus analysis (CMS)

The confirmation of possible electrode contribution, frequency proportionate capacitive effects, and temperature dependency of capacitance can be verified from the modulus plots concerning varying frequencies, at various discrete values of temperatures. The zero variation in M' values at low frequencies and at all temperatures, as depicted in Fig. 5a indicate zero electrode contributions [18, 19]. The mid-frequency dispersion M' may be attributed to the short-range hopping conduction and relaxation behavior [19–24]. The M'' vs. frequency plot as shown in Fig. 5b shows temperature-dependent relaxation mechanisms, whose maxima peaks correspond to the

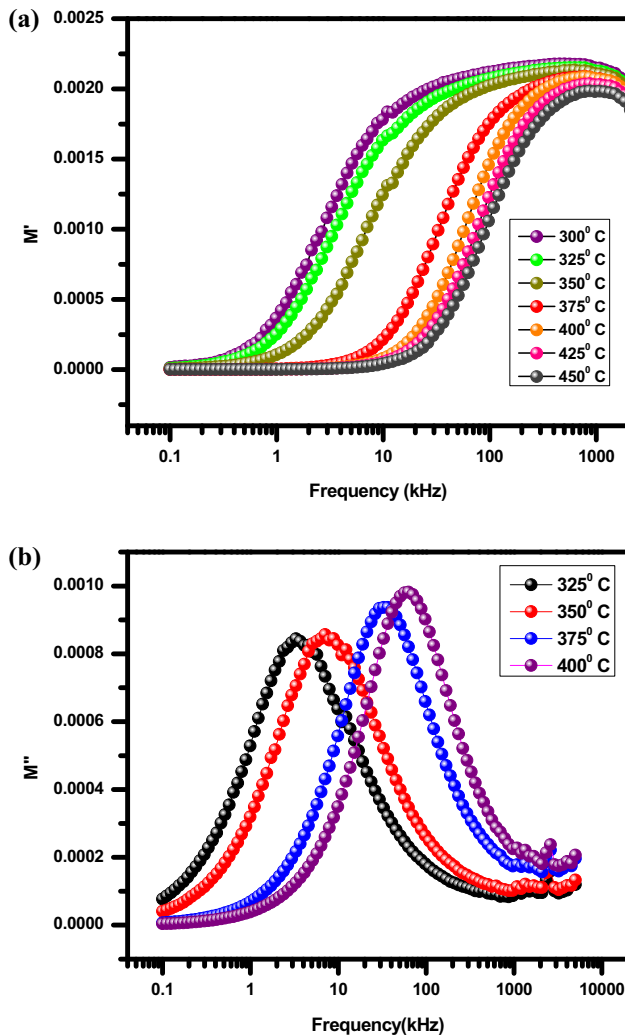


Fig. 5 a Real modulus vs. frequency. b Imaginary modulus against frequency

capacitive effects of the composite ceramic. The amplitude of the relaxation peaks keeps on increasing as the temperature rises indicating that the capacitive values increase with temperature. The relaxation times are again found to be decreasing with temperature rise since the maximas shift towards the right.

4.2 AC conductivity measurements

The frequency-dependent ac conductivity is enumerated in Fig. 6. The conductivity perfectly follows the Almond–West formalism [25] $\sigma(\omega) = \sigma_{dc} \left[1 + \omega^n / \omega_c^n \right]$ at lower and higher frequencies. In a low-frequency range, the conductivity is mainly contributed by σ_{dc} while in the high-frequency sweep; the conductivity is proportional to ω^n , where n and A are being temperature variant parameters. The conductivity values increase with the increase in temperature suggesting NTCR characteristics and the semiconducting nature of the sample. The enhancement in the slope values with temperature rise can be mainly attributed to the hopping phenomena between ferrite ions.

4.3 The J–E curve

The current density (J) against the electric field (E) is illustrated in Fig. 7, as a function of the applied electric field measured at room temperature. It gives us a measure of the overall insulating contribution

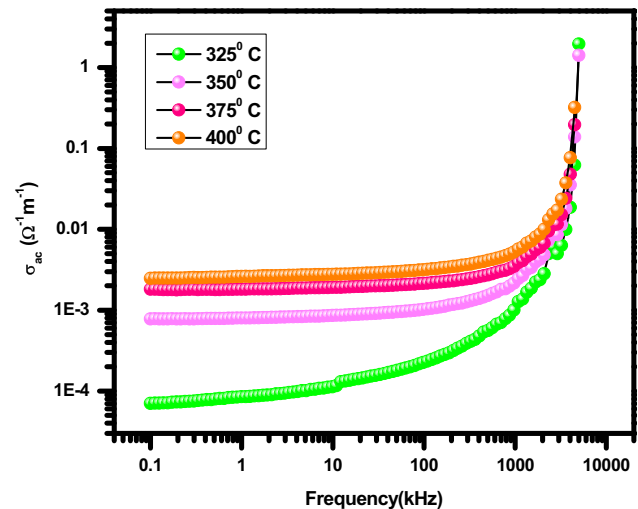


Fig. 6 Alternating current (AC) conductivity as a function of frequency

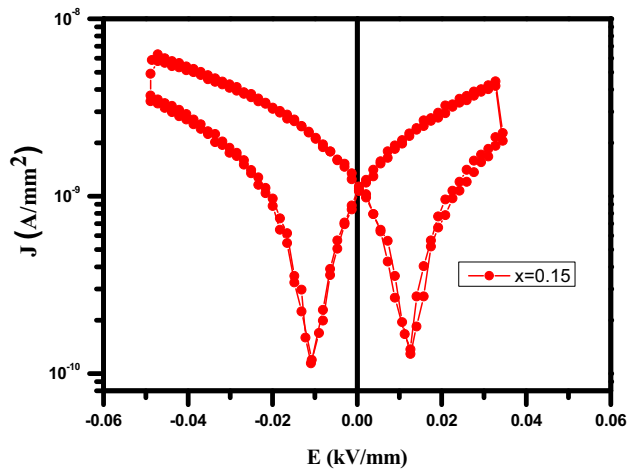


Fig. 7 The current density (J) vs. electric field (E)

from the compound. Since the leakage current density of the samples increases nonlinearly with the enhancing applied time-dependent electric field, this implies the sample's perfect relaxor behavior for energy storage utilities [26]. A similar characteristic is also exhibited by the sample when the applied field is reversed. The curves show a hysteresis kind of loop for both forward and reverse conditions implying a remnant polarization even at zero applied field. This property makes it useful for electrical energy storage device applications.

4.4 The polarization–electric field loop study

To investigate the multiferroic nature of a composite, it is very necessary to perform the ferro-electricity analysis using the P–E loop tracer method. Figure 8 depicts the P–E loop of the composite whereas

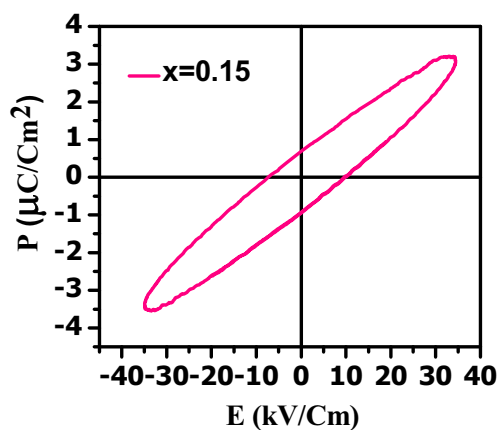


Fig. 8 The P–E loop

remnant polarization in the polarization vs. electric field hysteresis is clearly visible which ensures the presence of ferro-electricity in the studied compound and validates the sample's multiferroicity. The presence of leakage currents in the DPO ceramic does not allow the polarization to saturate which is why there is a blunt corner in the P–E loop. The volatile nature of Fe and Mg evaporation due to high temperature sintering may be held responsible for it [27]. Saturation in the closed PE curve is not seen at maximum applied voltage because of the low density formation of the polycrystalline sample. The +ve curvature observed in the polarization vs. field curve is another indication towards the ferroelectric behavior of the compound, making the compound possible for device applications.

4.5 Magnetization study from the M–H loop

A negligible hysteresis loop in the M–H curve is observed for the compound under investigation, as divulged from Fig. 9. It is observed to exhibit saturating ferromagnetization for large magnetic fields of the order of 1.9kOe. The extremely low coercivity value and small remnant magnetization points towards the weak ferromagnetic behavior of the sample. Existence of valency fluctuations of ferric ions (Fe^{3+} , Fe^{2+}) different spin states might have contributed feebly towards the saturation magnetic moment. Short-range ferromagnetic double interaction between the neighboring spin along the interaction chains, such as Fe^{3+} (or Fe^{2+})–O– Fe^{3+} or

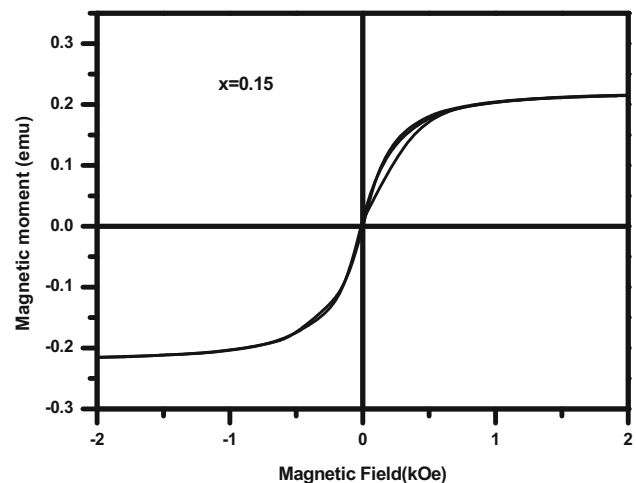


Fig. 9 The ambient temperature M–H loop

$\text{Nb}^{5+}-\text{O}-\text{Fe}^{3+}$ (or Fe^{2+}) can be held responsible for the weak magnetic properties [28, 29]. Also, crystallite size distributions have might be the reason behind low retentivity and coercivity values [30]. Hence, grain size variations and exchange interactions play a significant role in tuning the magnetic properties of the materials.

5 Conclusion

The structural analysis from the XRD analysis reveals the structure deformation to the orthorhombic group which has its own characteristics contributions towards the enhanced ferroelectric, dielectric and magnetic behavior. The frequency-dependent dielectric study reveals samples' large dielectric values at low frequencies for capacitive storage device applications. The NTCR nature as evident from the impedance analysis reveals the compound's potential semiconducting property. The CMS spectroscopy shows temperature-dependent enhancement in the capacitive and dielectric values in the sample. The tapered narrow band gap of the ceramic makes it possible for photovoltaic application. The presence of ferroelectricity and ferromagnetism is evidenced from the P–E and M–H loop tracers which proves that the compound is a multiferroic at room temperature where magnetism and ferroelectricity exist simultaneously in the single phase.

Author contributions

All authors contributed to the study conception and design. Material preparation, data collection and analysis were performed by [SM], [SS], [SB] and [BNP]. The first draft of the manuscript was written by [SM] and all authors commented on previous versions of the manuscript. All authors read and approved the final manuscript.

Funding

There is no funding applicable.

Data availability

Research data is not available in the manuscript and it will be available on the request.

Declarations

Competing interest The authors have no relevant financial or nonfinancial interests to disclose.

References

1. K. Leng, Q. Tang, Y. Wei, Li. Yang, Y. Xie, Wu. Zhiwei, X. Zhu, *AIP Adv.* **10**, 120701 (2020). <https://doi.org/10.1063/5.0031196>
2. Q. Tang, X. Zhu, *Nanomaterials* **12**, 224 (2022). <https://doi.org/10.3390/nano12020244>
3. P. Kayser, M.J. Martínez-Lope, J.A. Alonso, M. Retuerto, M. Croft, A. Ignatov, M.T. Fernández-Díaz, *Eur J Inorg Chem.* (2014). <https://doi.org/10.1002/ejic.201301080>
4. D.D. Khalyavin, J.P. Han, A.M. Senos, P.Q. Mantas, *Sci. Forum* **455**, 30–34 (2004). <https://doi.org/10.4028/www.scientific.net/msf.455-456.30>. (Trans Tech Publications, Ltd)
5. L. Skutina, E. Filonova, D. Medvedev, A. Maignan, *Cells. Mater.* **14**(7), 1715 (2021). <https://doi.org/10.3390/ma14071715>
6. R. VaradwajPradeep, H.M. Marques, *Front. Chem.* (2020). <https://doi.org/10.3389/fchem.2020.00796>
7. R.S. Lamba, P. Basera, S. Bhattacharya, S. Sapra, *Phys. Chem. Lett.* **10**(17), 5173–5181 (2019). <https://doi.org/10.1021/acs.jpcclett.9b02168>
8. Ilaria Carlomagno Abhisek Bandyopadhyay, M. Laura Simionelli, A.E. Moretti Sala, C. Meneghini, S. Ray, *Phys. Rev. B* **100**, 064416 (2019). <https://doi.org/10.1103/PhysRevB.100.064416>
9. I.D. Sayantika Bhowal, *Phys. Rev. B* **97**, 024406 (2018). <https://doi.org/10.1103/PhysRevB.97.024406>
10. N.V. Urusova, M.A. Semkin, E.A. Filonova, M. Kratochvilova, D.S. Neznakhin, J.-G. Park, A.N. Pirogov, *J. Phys.: Conf. Ser.* **1389**, 012131 (2019). <https://doi.org/10.1088/1742-6596/1389/1/012131>
11. M. Rabiei, A. Palevicius, A. Monshi, S. Nasiri, A. Vilkauskas, G. Janusas, *Nanomaterials* **10**(9), 1627 (2020). <https://doi.org/10.3390/nano10091627>
12. J. Smit, H.P.J. Wijn, *Adv. Electr. Electron Phys.* **6**, 69–136 (1954). [https://doi.org/10.1016/S0065-2539\(08\)60132-8](https://doi.org/10.1016/S0065-2539(08)60132-8)
13. K. Jawahar, R.N.P. Choudhary, *Matter. Lett.* **62**, 911 (2008)
14. C.G. Koops, *Phys. Rev.* **83**, 121 (1951). <https://doi.org/10.1103/PhysRev.83.121>

15. N. Rezlescu, E. Rezlescu, *Phys. Stat. Sol. A* **23**, 575 (1974). <https://doi.org/10.1002/pssa.2210230229>
16. S.H. Kim, K.D. Park, H.S. Lee, *Energies* **14**, 275 (2021). <https://doi.org/10.3390/en14020275>
17. D.K. Mahato, A. Dutta, T.P. Sinha, *Bull. Mater. Sci.* **34**(3), 455–462 (2011)
18. J.W. Chen, K.R. Chiou, A.C. Hsueh, C.R. Chang, *RSC Adv.* **9**, 12319–12324 (2019)
19. S. Pattanayak, B.N. Parida, P.R. Das, R.N.P. Choudhary, *Appl. Phys. A* **112**, 387–395 (2013)
20. J. Plochanski, W. Wiczorek, *Solid State Ion.* **28**, 979–982 (1982)
21. M.A.L. Nobre, S. Lanfredi, *J. Phys. Chem. Solid.* **62**, 1999 (2001)
22. S. Behera, B.N. Parida, P. Nayak, P.R. Das, *J. Mater. Sci. Mater. Electron.* **24**, 1132 (2013)
23. C.K. Suman, K. Prasad, R.N.P. Choudhary, *J. Mater. Sci.* **41**, 369 (2006)
24. T.S. Irvine, D.C. Sinclair, A.R. West, *Adv. Mater.* **2**, 132 (1990)
25. M. Siekierski, W. Wiczorek, *Solid State Ionics* **60**(1–3), 67–71 (1993). [https://doi.org/10.1016/0167-2738\(93\)90276-9](https://doi.org/10.1016/0167-2738(93)90276-9)
26. H. Yang, F. Yan, Y. Lin, T. Wang, F. Wang, *Sci. Rep.* **7**, 8726 (2017). <https://doi.org/10.1038/s41598-017-06966-7>
27. G. Blasse, *J. Chem. Phys.* **45**, 2356 (1966)
28. H.S. Kim, L. Bi, G.F. Dionne, C.A. Ross, H.J. Paik, *phys Rev. B.* **77**, 214436 (2008)
29. Z.X. Cheng, X.L. Wang, S.X. Dou, H. Kimura, K. Ozawa, *Phys. Rev. B* **77**, 092101 (2008)
30. C. Kursun, M. Gogebakan, E. Uludag, M.S. Bozgeyik, F.S. Uludag, *Sci. Rep.* **8**, 13083 (2018). <https://doi.org/10.1038/s41598-018-31458-7>

Publisher's Note Springer Nature remains neutral with regard to jurisdictional claims in published maps and institutional affiliations.

Springer Nature or its licensor holds exclusive rights to this article under a publishing agreement with the author(s) or other rightsholder(s); author self-archiving of the accepted manuscript version of this article is solely governed by the terms of such publishing agreement and applicable law.